Int. J. Electrochem. Sci., 11 **(2016)** 3512 - 3531

International Journal of
ELECTROCHEMICAL
SCIENCE
www.electrochemsci.org

Role of Yttrium Substitution in the Atomic Cluster Evolution and Corrosion Behaviour of Al-Ni-Gd Metallic Glasses

Y.G. Wang [1], *Y.J. Li* [1], *S.P. Pan* [2], *B.D. Fu* [1], *J. Y. Qin*[1], *W.M. Wang* [1,*]

[1] Key Laboratory for Liquid-Solid Structural Evolution and Processing of Materials, Ministry of Education, Shandong University, Jinan 250061, China
[2] Department of Material Science and Engineering, Taiyuan University of Technology, Taiyuan 030024, China
[*]E-mail: weiminw@sdu.edu.cn

Received: 30 January 2016 / *Accepted:* 2 March 2016 / *Published:* 1 April 2016

Atomic cluster evolution and corrosion behaviour of $Al_{84}Ni_{10}Gd_{6-x}Y_x$ (x = 0, 2, 4 and 6) metallic glasses were investigated using experimental methods and *ab initio* molecular dynamic simulations. The shoulder peak area in x-ray diffraction patterns, enthalpy of second and third crystallization and population of <0 3 6 0> Ni-centered clusters increase with increasing yttrium content, but the onset temperature and enthalpy of first crystallization decrease simultaneously. Yttrium substitution and annealing treatment can aggravate metastable pitting and induce a thicker alumina film during polarization, which can be explained by the segregation of Ni-centered clusters and ordering of Al-rich clusters.

Keywords: Metallic glass; Al alloy; Corrosion; Pitting.

1. INTRODUCTION

Al-based metallic glasses (MGs) with aluminum content over 80 at.% exhibit an extremely good corrosion resistance combined with high strength and have potential applications such as metal coatings [1]. These excellent properties are ascribed to the chemical and structural homogeneity of the metastable amorphous structure. However, the presence of short range orders (SROs) and medium range orders (MROs) in the glasses is unavoidable, which has a great influence on the mechanical and electrochemical properties [2]. Hence, understanding the effects of SRO or atomic clusters on the corrosion properties becomes of essential importance.

To uncover the structure characters of Al-based MGs, many experimental works were carried out, e.g., by using X-ray absorption spectroscopy, Mansour et al. revealed the Al-Co bond in Al-Co-Ce

doi: 10.20964/110429

MGs has a covalently bonded environment [3]; by using high energy X-ray diffraction (XRD), our recent work observed that there is a shoulder peak in the Al-Ni-Gd MGs [4]. Nevertheless, the detailed atomic structure especially for the evolution of atomic clusters is still unclear. Recently, *ab initio* molecular dynamics (AIMD) simulations have been used to investigate the structure characters for Al-based metallic glasses. The AIMD simulations show that the properties of Al-based MGs are mainly dependent on the solute-centered quasi-equivalent clusters [5]. Poon et al. [6] also proposed the backbone model that the backbone clusters in Al-based MGs can stabilize the amorphous structure and improve the glass forming ability (GFA). Hence, here comes the question, how to strengthen the backbone clusters and tune the properties of the Al-based MGs? Han et al. [7] pointed out that addition of Ce can enhance the GFA of Al-Fe MGs. Our earlier work [8] also found that the addition of Ni can improve the GFA and corrosion resistance of the Al-Ni-Gd MGs. Although several ways to improving corrosion resistance in Al-based MGs are discovered, the insight of the structural evolution by the substitution of rare earth elements in Al-based MGs has not been concerned.

Annealing treatment can bring great influence on the structure and properties of MGs [9, 10]. In the case of annealed Al-Co-Ce MGs, the bond length of Al-Co and Al-Ce is decreased and the corrosion resistance is declined [7]. Hence, we need to understand the internal mechanism of the annealing treatment on the amorphous structure. As shown in Ref. [11], the devitrification of face centered cubic Al (fcc-Al), as a result of the annealing can greatly affect the metastable pitting corrosion behaviour of Al-based MGs. This mechanism has not been reported in the literature which may give a further understanding of the effect of annealing on the corrosion resistance.

In our earlier work, the metastable pitting (P_{mp}) was observed in Al-Ni-Gd MGs [8]. We found that the addition of Ni can enhance the P_{mp} which is ascribed to the stress between the Ni-rich corroded part and uncorroded part. In this paper, we intend to investigate the role of Y substitution on the evolution of the Al(Ni)-rich clusters in the Al-based MGs, hope to further understand the metastable pitting process which is helpful to develop a promising Al-based MG with good corrosion resistance.

2. EXPERIMENTAL AND AIMD SIMULATION

The ingots of $Al_{84}Ni_{10}Gd_{6-x}Y_x$ (x = 0, 2, 4 and 6) were prepared by high frequency induction-melting pure Al, Ni, Gd and Y materials (purity > 99.9 wt.%) in the air. The ribbons were prepared by a single-roller melt-spinning equipment in the air at the circumferential speed of 29.3 m/s. The parameters such as the melt speed, the injection pressure are kept constant during the spinning process. The amorphous or crystalline state of the as-spun and annealed ribbons were characterized by X-ray diffractometer (XRD) with a D/Max-rB diffractometer with Cu Kα radiation. The thermal analysis of as-spun ribbon was performed using a differential scanning calorimetry (DSC) (Netzsch DSC 404) under an Ar atmosphere from room temperature to 500°C with a heating rate of 10 K/min. The ribbons were annealed in a silicon crucible in an Ar atmosphere and the annealing temperature was chosen as 290°C (this temperature is well above the first crystallization ending temperature) according to the DSC data. The wheel surface morphology and phase images of the as-spun and annealed sample were performed using atomic force microscope (AFM, Bruker Dimension Icon). The test was carried out in the tapping mode with a scanning rate of 2.0 line/s. A silicon cantilever with soft tapping mode tip was used. The samples used for AFM test were ground in sequence on 800, 1400, 2000 grit SiC paper and then polished with 1 μm diamond paste using the deionized water as the lubricant. They were subsequently ultrasonically cleaned by deionised water.

The electrochemical measurements were carried out using potentiodynamic polarization technique. The electrochemical tests were performed using a typical three-electrode system, using a platinum plate as the counter electrode and a saturated calomel electrode (SCE) as the reference electrode. All measurements were performed using a CHI660E electrochemical workstation in a free exposed 3.5 wt.% NaCl solution at 25 °C. All specimens were immersed in the electrolyte for 20 min prior to the potentiodynamic polarization test to stabilize their open circuit potentials (OCP). After the polarization test, the samples were ultrasonically cleaned two times in deionized water and air-dried. Here, we have to clarify that in our earlier work the polarization curves was measured by twice scanning process and the scanning rate was 5 mV/s [8]. In this research, we measured the polarization curves with only one scanning process and the scanning rate was 1 mV/s; to clarify the formation of current peak, the polarization of the as-spun sample with c_{Y} = 6 at.% is scanned at a rate of 0.1 mV/s after a H_2SO_4 passivation pretreatment on CS310 electrochemical station (Wuhan Corrtest Instrument Company, being the same company in Ref. [12]) . The surface morphology of the samples after full potentiodynamic polarization as well as polarization till the end of current peak were examined by scanning electron microscopy (SEM, HITACHI SU-70). The surface films of the corroded samples were analyzed by X-ray photoelectron spectrometer (XPS, ESCALAB 250Xi). The binding energy scale was calibrated using C 1s peak of the contaminated surface carbon that corresponds to 284.6 eV. The measured peaks were fitted using the XPS Peak software and the deviation is below 1%. The quantitative data of the surface elements was achieved by the Avantage 5.52 software.

Ab initio molecular dynamic (AIMD) simulations are analyzed on the basis of the density functional theory using Vienna *ab initio* simulation package (VASP) [13] by implementing the projector augmented vave method [14]. All dynamical simulations were carried out in a canonical ensemble (NVT) through Nosé thermostat to control temperature [15]. Cubic cells containing 100 atoms with periodic boundary condition were used to simulate the liquid and glassy $Al_{84}Ni_{10}Gd_{6-x}Y_x$ (x = 0 and 6) alloys. The initial structures are equilibrated at 2000 K, which is well above the melting temperature of the alloy. After sufficiently relaxed for 4000 steps, the alloys are cooled down from 1500 K to 300 K at the rate of 10^{15} K/s to produce amorphous solids. At each temperature, the last 3000 configurations are used for analysis. The data of 1500 K melts and 300 K glasses are chosen in this research for the structure analysis. The partial pair distribution function ($g_{\mathrm{ij}}(r)$) represents the probability to find an i atom in the shell Δr at the distance r of another j atom, the calculating detail of which is shown in Ref. [7].

3. RESULTS

The XRD patterns and DSC curves of as-spun $Al_{84}Ni_{10}Gd_{6-x}Y_x$($x$ = 0, 2, 4 and 6) samples are shown in Fig. 1. Only a broad diffraction peak can be found in the XRD patterns (Fig. 1a), which implies the amorphous structure of four as-spun samples. In addition, a slight shoulder peak which is outlined by a Gaussian fitting can be found near the main peak and its intensity increases with increasing the yttrium content c_Y. In DSC curves (Fig. 1b), no distinct glass transition is found and three exothermal peaks corresponding to three crystallization reactions appear in the heating process between 200~400 °C.

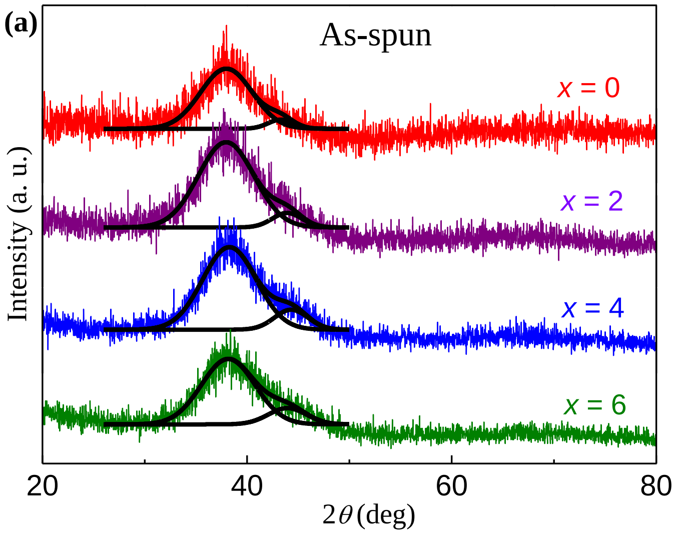

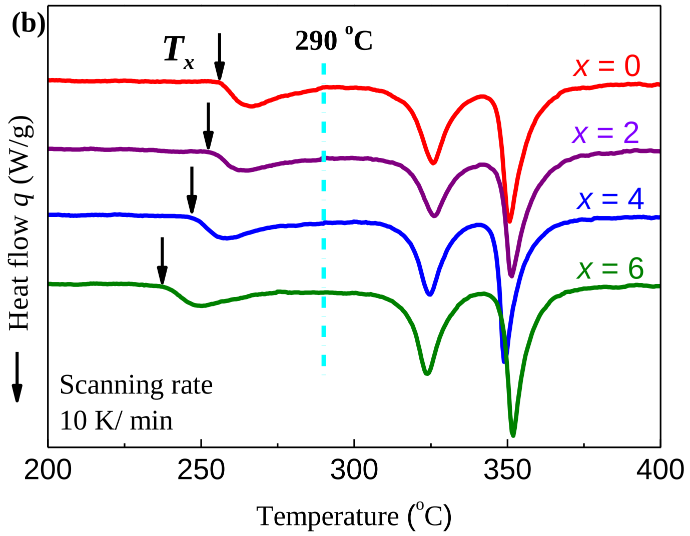

Figure 1. (a) XRD and (b) DSC curves of the as-spun $Al_{84}Ni_{10}Gd_{(6-x)}Y_x$ (x = 0, 2, 4 and 6) glassy ribbons.

The first wide exothermal reaction in 240~285 °C corresponds to fcc-Al nanocrystals formation, while the second and third exothermal reactions are often relative to the formation of the intermetallic compounds according to earlier works [16, 17]. The area of shoulder peaks in XRD (A_{shoulder}), parameters in DSC curves and thickness of ribbons are listed in Table 1. Opposite to the A_{shoulder} of four samples, the onset temperature of first crystallization peak (T_{x1}) decreases with increasing c_Y. The area of first exothermic peak (ΔH_1) decreases with increasing c_Y, but the area of second and third exothermic peaks (ΔH_2+ΔH_3) have a slight increasing tendency simultaneously. It is indicated that the addition of Y can facilitate the formation of fcc-Al and hinder the formation of the intermetallic compounds. Besides, the thickness of the ribbons increases with Y substitution, indicating that the viscosity of the melt increases.

Table 1. Areas of shoulder peak (A_{Shoulder}) in XRD, onset temperatures of crystallization and areas of exothermic peaks (T_x, ΔH_1 and $\Delta H_{2+}\Delta H_3$) in DSC as well as the thickness of the ribbons of $Al_{84}Ni_{10}Gd_{6-x}Y_x$ (x = 0, 2, 4 and 6) glasses.

Sample	**A_{Shoulder} in XRD (cps·deg)**	**DSC**			**Thickness (μm)**
		T_x (°C)	**ΔH_1 (J/g)**	**$\Delta H_{2+}\Delta H_3$ (J/g)**	
x = 0	20.5	256.1	23.1	97.4	14.3
x = 2	41.2	252.6	22.6	97.9	15.2
x = 4	58.3	247.0	22.5	98.0	22.8
x = 6	59.8	237.4	22.4	100.4	24.0

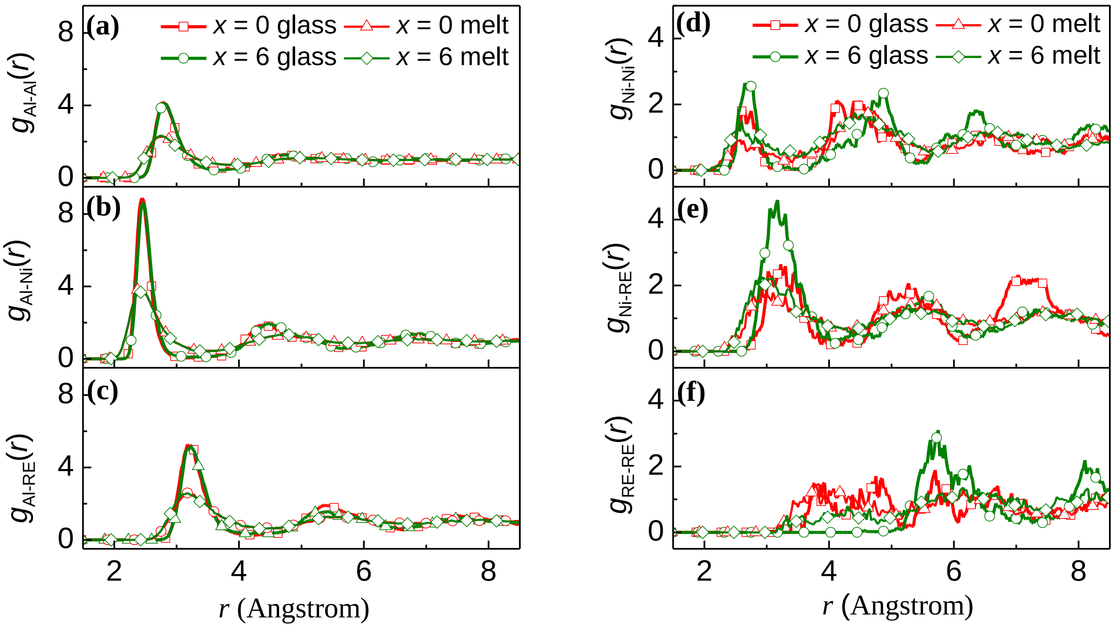

Figure 2. Partial pair distribution functions $g(r)$ of $Al_{84}Ni_{10}Gd_{(6\text{-}x)}Y_x$ (x = 0 and 6) glasses and melts.

Fig. 2 gives the partial pair distribution functions $g(r)$ of $Al_{84}Ni_{10}Gd_{6\text{-}x}Y_x$ (x = 0 and 6) alloys in glassy state at 300 K and in melt state at 1500 K. Owing to the low Ni and rare earth elements (RE = Gd or Y) contents, the $g_{\mathrm{Ni\text{-}Ni}}(r)$, $g_{\mathrm{Ni\text{-}RE}}(r)$, $g_{\mathrm{RE\text{-}RE}}(r)$ curves have a larger roughness than the other curves. The central position r_{max} and height $g_{A\text{-}A}(r_{max})$ of the first peak of $g_{A\text{-}A}(r)$ reflect the nearest neighbor distance and bond number of A-A atomic pair, respectively. The r_{max} and $g(r_{max})$ as well as the r_{max} change (Δr) between the melts and glasses deduced from partial $g(r)$ curves are shown in Table 2.

Table 2. The nearest first neighbor distances (r_{max}) and height of the first peaks (g(r_{max})) of partial $g(r)$ together with the variation of r_{max} of glasses cooling from the melts (Δr_{max}) of $Al_{84}Ni_{10}Gd_{6\text{-}x}Y_x$ (x = 0 and 6) alloys.

State	**Atomic bonds**	***x* = 0**			***x* = 6**		
		r_{max}(Å)	**Δr_{max}(Å)**	**$g(r_{max})$**	**r_{max}(Å)**	**Δr_{max}(Å)**	**$g(r_{max})$**
Glass	**Al-Al**	2.78	0.0	4.18	2.80	-0.05	4.10
	Al-Ni	2.45	-0.03	8.88	2.48	-0.04	8.61
	Al-RE	3.18	-0.00	5.20	3.23	-0.06	5.19
	Ni-Ni	2.65	-0.07	1.84	2.73	-0.13	2.71
	Ni-RE	3.23	-0.30	2.64	3.18	-0.28	4.60
Melt	**Al-Al**	2.78		2.27	2.74		2.34
	Al-Ni	2.42		3.91	2.44		3.80
	Al-RE	3.18		2.58	3.17		2.60
	Ni-Ni	2.58		0.94	2.60		1.51
	Ni-RE	2.93		1.95	2.90		2.31

Here, $\Delta r = r_{max}(\text{melt}) - r_{max}(\text{glass})$. Apparently, $g_{Al\text{-}Ni}(r_{max})$ is the highest among all atomic bonds, suggesting that the Ni-centered clusters are dominated clusters in the glasses and melts. In glass state, Y substitution has little effect on the $g_{Al\text{-}Al}(r_{max})$, $g_{Al\text{-}Ni}(r_{max})$ and $g_{Al\text{-}RE}(r_{max})$.

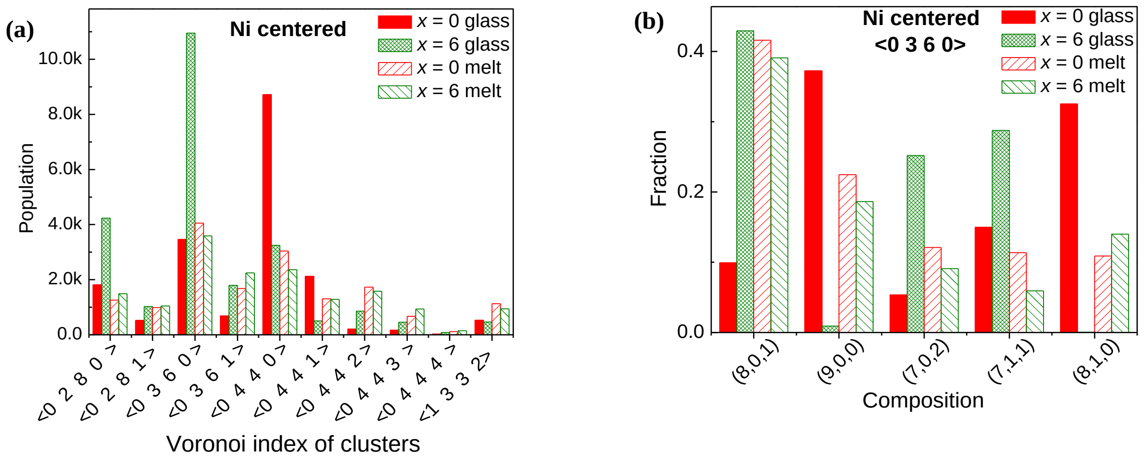

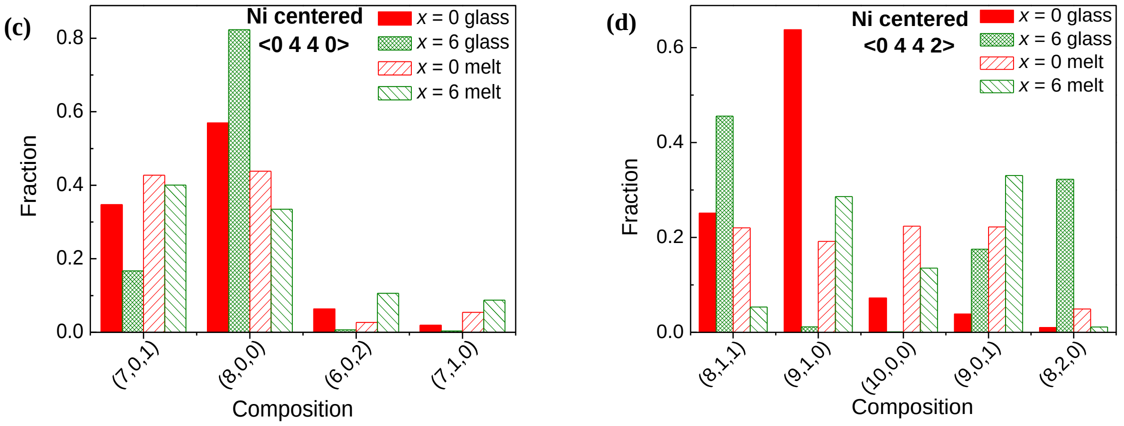

Figure 3. Population of Ni-centered Voronoi polyhedra and the distribution of various nearest neighboring atom composition in $Al_{84}Ni_{10}Gd_{(6-x)}Y_x$ (x = 0 and 6) glasses and melts. (a) Total population, (b) distribution of <0 3 6 0> clusters, (c) distribution of <0 4 4 0> clusters, and (d) distribution of <0 4 4 2> clusters.

However, the glass with c_Y = 6 at.% has a much higher $g_{\text{Ni-Ni}}(r_{\max})$ and $g_{\text{Ni-RE}}(r_{\max})$ than that with c_Y = 0, which indicates that Y substitution can increase the number of Ni-Ni and Ni-RE bonds. Meantime, we can find that the $\Delta r_{\max}$ of first four bonds of the alloy with c_Y = 6 at.% is more negative than that with c_Y = 0, indicating an abnormal expansion of these bonds in the sample with c_Y = 6 at.% during the solidification.

The Voronoi polyhedron analysis is used to characterize the clusters and the Voronoi polyhedron index is shown as $<n_3\ n_4\ n_5\ n_6>$, where n_i denotes the number of i-edged faces of the Voronoi polyhedron. The coordinate number Z is approximately equal to $n_3+n_4+n_5+n_6$ with ignoring the small n_7 or n_8. Meantime, the composition index (m_1, m_2, m_3) for the nearest neighboring shell of a given polyhedron denotes the number of Al, Ni and RE atoms, respectively.

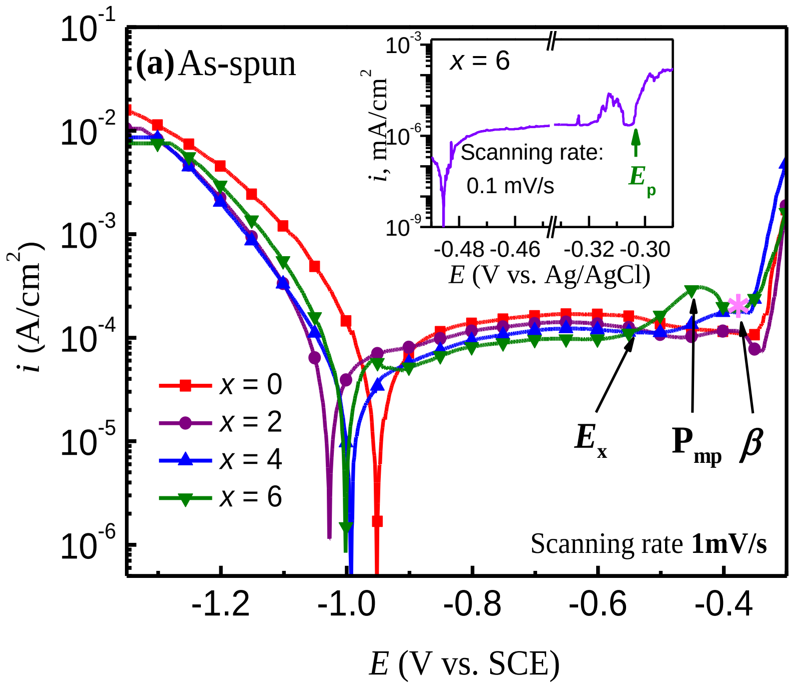

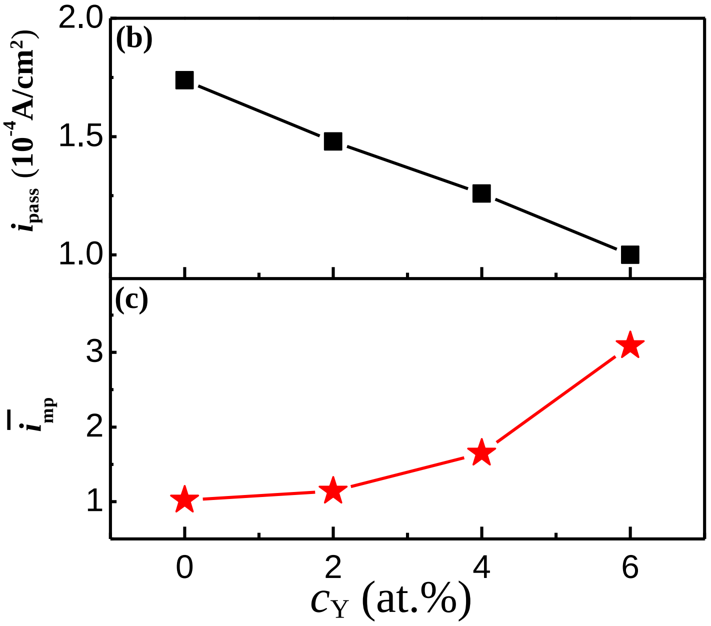

Figure 4. (a) Potentiodynamic polarization curves of as-spun $Al_{84}Ni_{10}Gd_{(6-x)}Y_x$ (x = 0, 2, 4 and 6) glassy ribbons together with the corresponding (b) the logarithm of passive current density i_{pass} and (c) reduced current density of the metastable pitting $\bar{i}_{mp}$. Inset in (a) is the potentodynamic polarization curves of sample with x = 6 under a scanning rate of 0.1 mV/s. P_{mp} denotes the current peak, and E_x and β denoted by star indicate the onset and end of P_{mp}.

The Voronoi indexes of Ni-centered clusters and the detailed composition distributions of dominated Ni-centered clusters are given in Fig. 3. In Fig. 3a, the tricapped trigonal prism (TTP) <0 3 6 0> clusters possess the highest population in the Ni-centered clusters and the population in the glass with c_Y = 6 at.% is much higher than that with c_Y = 0. The <0 4 4 0> and <0 4 4 2> clusters are distorted TTP clusters [18].

In glass state, the fraction of <0 3 6 0> cluster with a RE atom in the alloy with c_Y = 6 at.% is higher than that with c_Y = 0 (Fig. 3b), similar situation is found in <0 4 4 2> clusters (Fig. 3d), but the situation in <0 4 4 0> clusters is opposite (Fig. 3c). Apparently, the coordinate number Z of <0 4 4 2> cluster (Z = 10) is higher, but the Z of <0 4 4 0> cluster (Z = 8) is lower than that of the regular <0 3 6 0> TTP cluster. Consequently, the Y substitution in Al-Ni-Gd glasses can increase the Z of the Ni-centered clusters.

Fig. 4 displays the potentiodynamic polarization curves and the corresponding polarization parameters of as-spun $Al_{84}Ni_{10}Gd_{6-x}Y_x$ (x = 0, 2, 4 and 6) samples in 3.5 wt.% NaCl solution. In case of a scanning rate of 1 mV/s, the as-spun samples have a wide passive region (Fig. 4a). With increasing c_Y, the passivation current density (i_{pass}) of as-spun samples has a linear decreasing tendency (Fig. 4b), which indicates that Y substitution can increase the thickness of passive film.

Meanwhile, a current density peak is appeared at -0.5 to -0.25 V_{SCE}, denoted by P_{mp} and ended at β, reflecting the metastable pitting events in our earlier work [8]. To clarify the relationship between the current density peak and metastable pitting, we investigate the polarization curves of the alloy with c_Y = 6 at.% at a scanning rate of 0.1 mV/s, see inset in Fig. 4a. Apparently, there exist the metastable pitting transients in the measured polarization curve, the number of which rises with increasing the potential; below the pitting potential, the current transients overlap and appear as a “cluster”, being consistent with the results in Refs. [12, 19]. In addition, the current transients rise slowly but decay quickly, showing that the metastable pits have a difficult nucleation and an easy repassivation, similar to the current spike of stainless steel [20] and amorphous Ni-based alloy [21]. Meanwhile, we scale the height of P_{mp} by its reduced current density, $\overline{i}_{mp} = i_{mp}/i_{bg}$. Here, i_{mp} is the maximal current density of P_{mp}, and i_{bg} is the current density of its background.

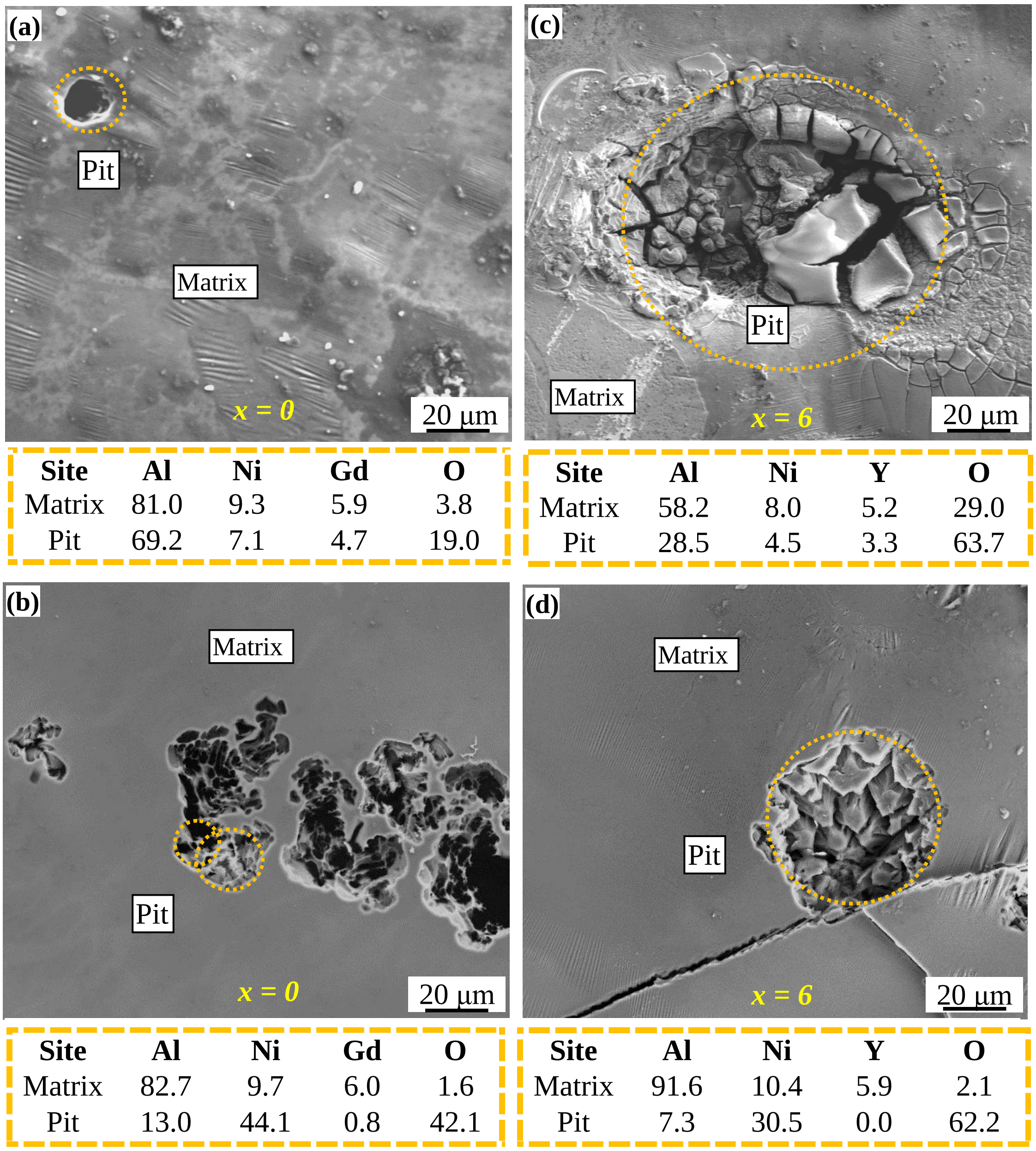

(a)

Site	Al	Ni	Gd	O
Matrix	81.0	9.3	5.9	3.8
Pit	69.2	7.1	4.7	19.0

(c)

Site	Al	Ni	Y	O
Matrix	58.2	8.0	5.2	29.0
Pit	28.5	4.5	3.3	63.7

(b)

Site	Al	Ni	Gd	O
Matrix	82.7	9.7	6.0	1.6
Pit	13.0	44.1	0.8	42.1

(d)

Site	Al	Ni	Y	O
Matrix	91.6	10.4	5.9	2.1
Pit	7.3	30.5	0.0	62.2

Figure 5. SEM micrographs of the corroded free surface of $Al_{84}Ni_{10}Gd_{6-x}Y_x$ glassy alloys together with EDS results. (a) Sample with $x = 0$ after polarized till β point, (b) sample with $x = 0$ after fully polarized, (c) sample with $x = 6$ after polarized till β point, and (d) sample with $x = 6$ after fully polarized; the insets show the element concentrations of pit and matrix positions in at.%.

The variation of $\bar{i}_{\mathrm{mp}}$ reveals an increasing tendency with increasing c_{Y} (Fig. 4c), while the onset potential of P_{mp}, E_{x}, decreases simultaneously (Fig. 4a), revealing that the metastable pitting of measured samples becomes heavier with yttrium substitution.

Fig. 5 shows the SEM micrographs of the corroded $\mathrm{Al}_{84}\mathrm{Ni}_{10}\mathrm{Gd}_{6\text{-}x}\mathrm{Y}_x$ glassy alloys after a full polarization and polarization till the end of P_{mp} (β point in Fig. 4a). For the sample with $c_{\mathrm{Y}} = 0$, the number of the pits in the ribbon polarized till β point is less than the fully polarized sample, and the pits in the latter contact each other and form several clusters; meanwhile, there exist some pits in diameter of 10 μm with some cracks (Fig. 5a and b). For the sample with c_{Y} = 6 at.%, there exist cracks inside the pit and some traces left by cracking in the sample after polarized till β point and larger "folk-like" cracks emitted from the pit in case of full polarization (Fig. 5c and d). Apparently, the number of cracks has an increasing tendency with increasing c_{Y}, which reflects a higher inner stress [8]. It can be found that nickel is enriched in pits in the samples after full polarization. The matrix has a higher oxygen content for the sample with c_{Y} = 6 at.%, which indicates that the Y addition sample has a thicker oxide film (insets in Fig. 5). Moreover, it can be clearly seen that the sample with c_{Y} = 6 at.% is thicker than the sample with $c_{\mathrm{Y}} = 0$, which is consistent with the result measured by screw micrometer (Table 1). The size of flower-like cracks and their area in sample with c_{Y} = 6 at.% are larger compared with $c_{\mathrm{Y}} = 0$. These results indicate that the sample with c_{Y} = 6 at.% possesses a larger corrosion stress than that with $c_{\mathrm{Y}} = 0$.

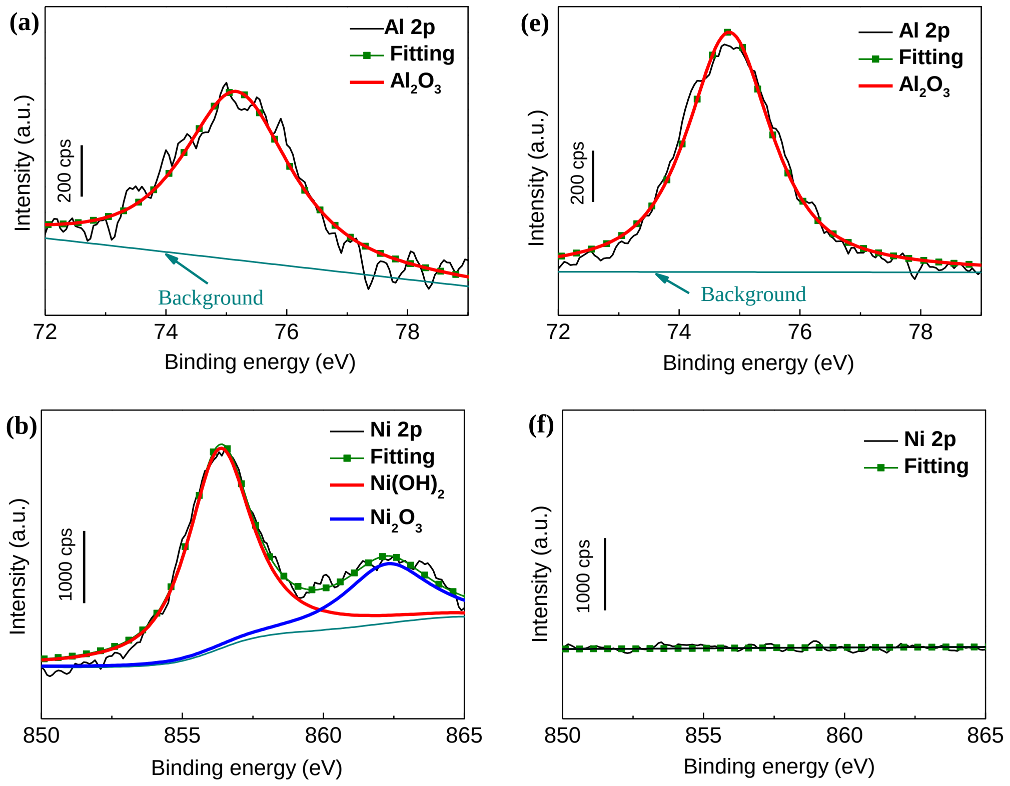

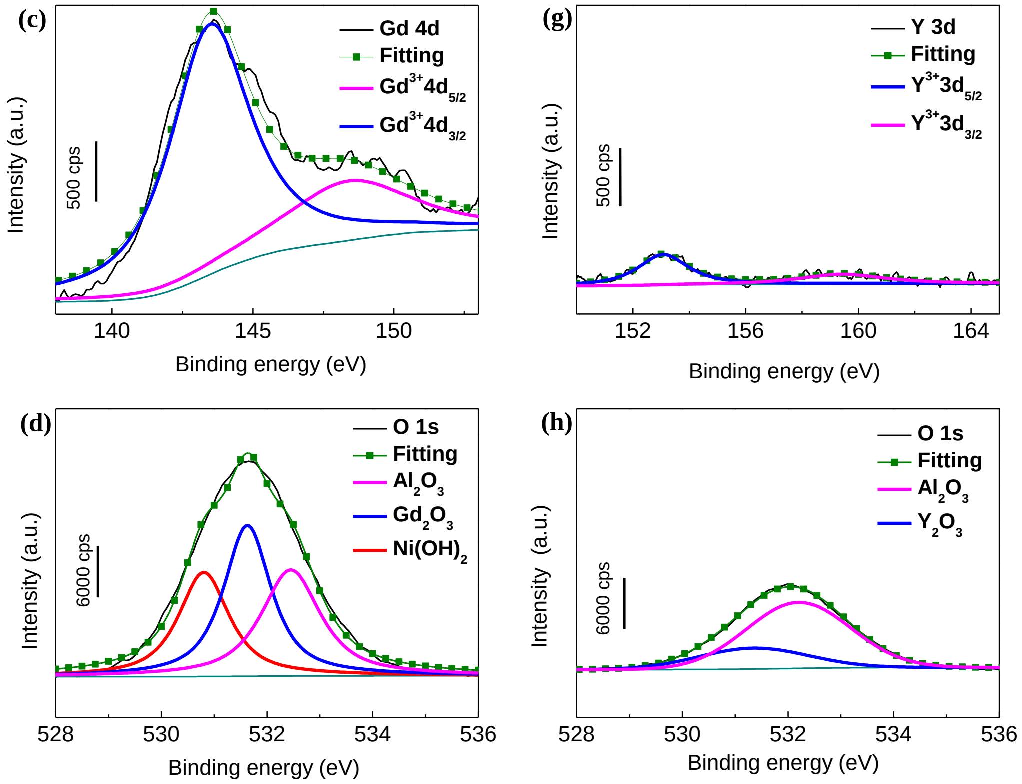

Figure 6. Al 2p, Ni 2p, Gd 4d, Y 3d and O 1s XPS spectrum as well as the fitting peaks of corroded as-spun $Al_{84}Ni_{10}Gd_{6-x}Y_x$ (x = 0 and 6) glassy alloys after full polarization. (a-d) x = 0; (e-h) x = 6.

In order to provide more information about the passive film formed during the electrochemical test, the XPS technique was employed on the $Al_{84}Ni_{10}Gd_{6-x}Y_x$ (x = 0 and 6) glassy alloys after polarization. Fig. 6 gives the Al 2p, Ni 2p, Gd 4d, Y 3d and O 1s spectrums of the samples after full electrochemical polarization. The corresponding element concentrations obtained from the XPS survey are listed in Table 3.

Table 3. Relative atomic concentrations on the electrochemical corroded surface of as-spun and annealed $Al_{84}Ni_{10}Gd_{6-x}Y_x$ (x = 0, 4 and 6) glasses obtained from XPS.

State	Sample	c_{Al} (at.%)	c_{Ni} (at.%)	c_{Gd} (at.%)	c_Y (at.%)	c_O (at.%)
As-spun	**x = 0**	23.39	2.96	3.64	-	70.01
	x = 4	25.10	1.15	1.62	1.00	71.13
	x = 6	26.00	0.26	-	1.21	72.53
Annealed	**x = 0**	25.92	0.87	2.23	-	70.98

The XPS spectrums of the as-spun sample with c_Y = 4 at.% and annealed sample with c_Y = 0 are not given here. The Al 2p spectrum of both samples can be fitted by the peak of alumina (Al_2O_3).

The Al 2p peak of sample with c_Y = 6 at.% is higher than that with c_Y = 0, which indicates that the Y substitution can supply more activated Al atoms to participate in the passivation and form a thicker alumina film on the surface. The Ni 2p spectrum of the sample with c_Y = 0 can be divided into two components, Ni^{+2} in ($Ni(OH)_2$) and Ni^{+3} in (Ni_2O_3), while the Ni 2p peak is absent on the surface of the sample with c_Y = 6 at.%. Similarly, the sample with c_Y = 6 at.% show a weaker RE signal than that with c_Y = 0. Meantime, the O 1s peak can be divided into two categories: the alumina peak and the solute element oxide peak. Though the sample with c_Y = 6 at.% does not contain the $Ni(OH)_2$ peak, it has a higher O content than that with c_Y = 0; meantime, the O content deduced from XPS spectrum has a linear increment with the Y addition (Table 3). These facts suggest that the thicker alumina passive film on the surface covers more signal of the nickel and rare earth elements. In addition, the increased O content and the absent of Ni 2p peak in XPS spectrum are also found for the annealed sample (Table 3), indicating that a thicker alumina passive film has formed after annealing treatment.

The XRD patterns and potentiodynamic polarization curves of annealed $Al_{84}Ni_{10}Gd_{6-x}Y_x$($x$ = 0, 2, 4 and 6) samples are shown in Fig. 7.

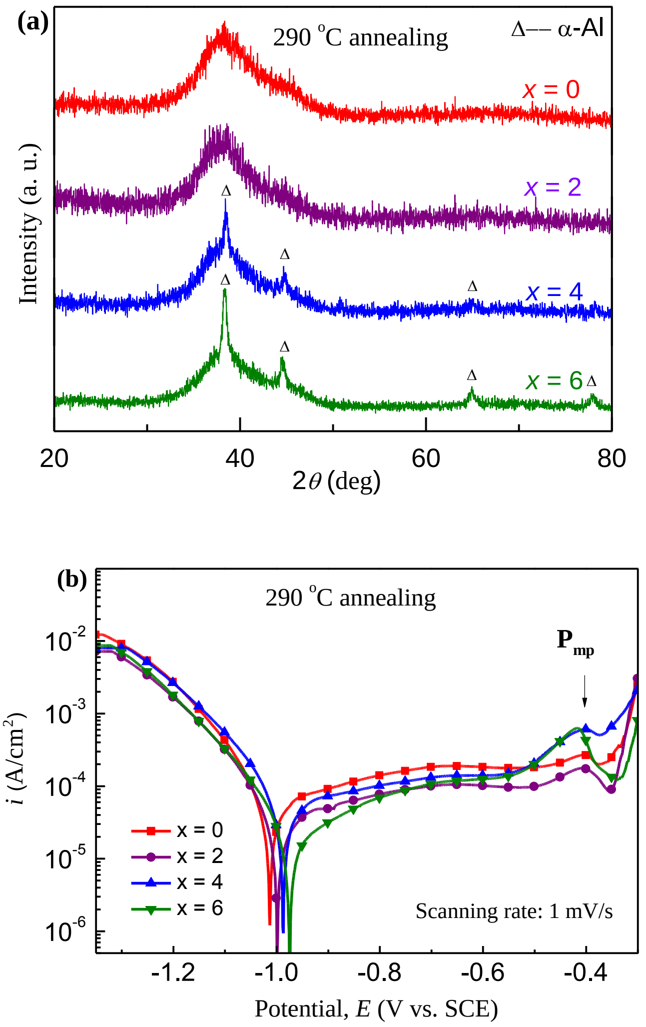

Figure 7. (a) XRD patterns and (b) potentiodynamic polarization curves of the annealed $Al_{84}Ni_{10}Gd_{(6-x)}Y_x$ (x = 0, 2, 4 and 6) glassy alloys.

After annealed at 290 °C for 5 min, the sharp crystalline peaks of fcc-Al appear on the XRD patterns of the samples with c_Y = 4 and 6 at.%, and the intensity increases with c_Y, which is consistent with the DSC result (Fig. 1b). Similar to as-spun ribbons, all annealed samples have a wide passive region. Moreover, the metastable pitting peak P_{mp} is also found in the annealed samples and becomes heavier than that in case of as-spun samples. The P_{mp} parameters of the as-spun and annealed samples are shown in Table 4.

Table 4. The onset potential E_x and reduced current density $\bar{i}_{mp}$ of the P_{mp} in the potentiodynamic polarization curves of as-spun and annealed $Al_{84}Ni_{10}Gd_{(6-x)}Y_x$ (x = 0, 2, 4 and 6) glasses.

Sample	**As-spun**		**Annealed**	
	E_x(V_{SCE})	**$\bar{i}_{mp}$**	**E_x (V_{SCE})**	**$\bar{i}_{mp}$**
$x = 0$	-0.45	1.02	-0.51	1.47
$x = 2$	-0.48	1.14	-0.52	1.77
$x = 4$	-0.53	1.65	-0.58	4.36
$x = 6$	-0.59	3.09	-0.61	5.24

For two types samples, the onset potential of P_{mp}, E_x, tends to be more negative with increasing c_Y, while their reduced current density $\bar{i}_{mp}$ increases on the opposite. In addition, the annealing treatment can decrease the E_x of sample but increase its $\bar{i}_{mp}$ simultaneously. That is to say, both Y substitution and annealing treatment can enhance the metastable pitting.

Fig. 8 presents the 1×1 μm AFM topography and phase images of the as-spun and annealed $Al_{84}Ni_{10}Gd_6$ amorphous alloys. The topography images reveal that the surface of the as-spun sample with the height fluctuation within 25 nm is flatter than the annealed one with the height fluctuation within 45 nm (Fig. 8a and c). The dark and bright zones of as-spun sample tend to segregate or grow after annealing treatment in the topography images. Similarly, both dark spot and bright zone in the phase image of as-spun sample tend to grow and the corresponding phase shift increases after the annealing treatment (Fig. 8b and d). Magonov et al. [22] proposed that a darker region in the phase image with a more negative phase shift is related to a softer surface. Zhang et al. also confirms that the dark spots in phase images of $Al_{88}Ni_6Ce_4$ metallic glass is soft fcc-Al phase [11]. Accordingly, the dark spots in the phase images can be regarded as Al-rich region in present glasses with the bright zone being Ni-rich region. Obviously, the growth of Al-rich region after annealing treatment indicates that the annealing treatment increases the order of the Al-rich clusters. In other words, the structure heterogeneity is increased after annealing treatment.

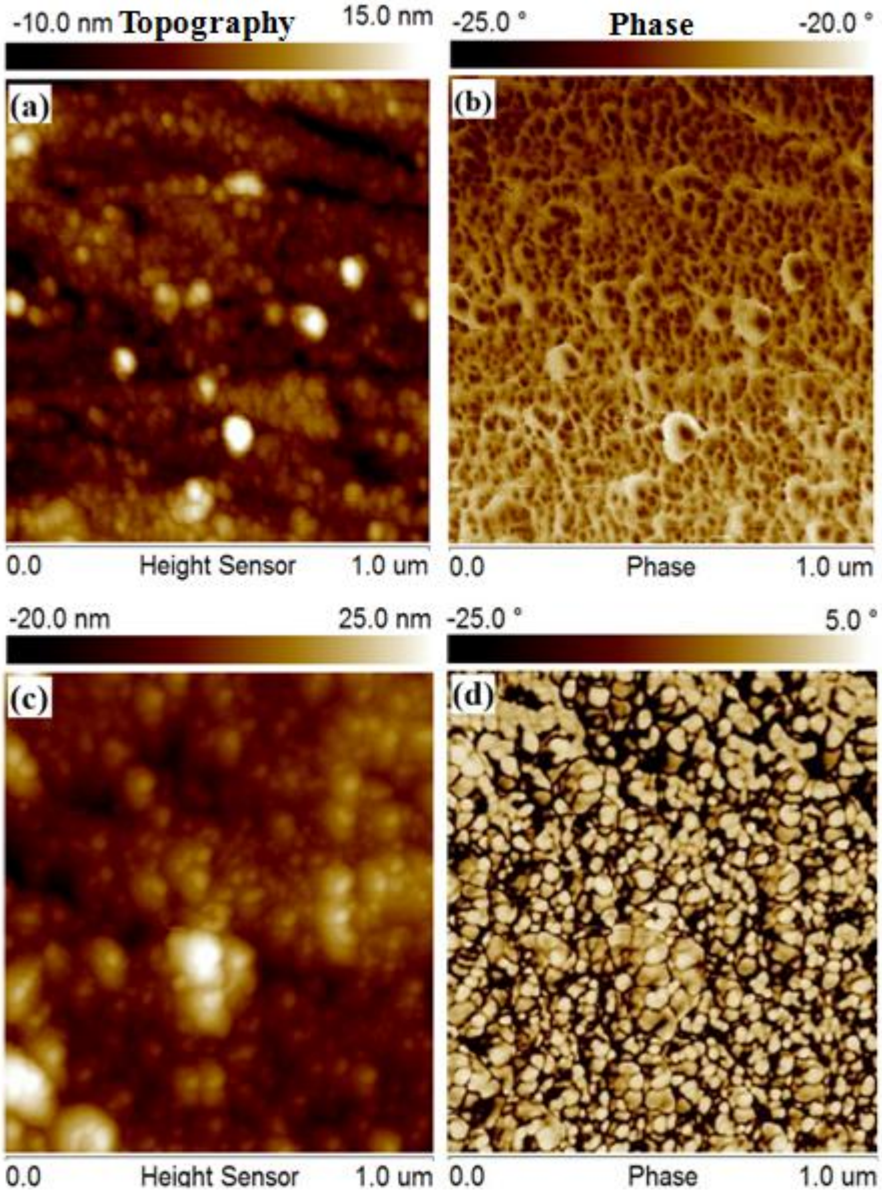

Figure 8. AFM images of topography and phase for as-spun and annealed $Al_{84}Ni_{10}Gd_6$ glassy alloy. (a) topography of as-spun sample, (b) phase of as-spun sample, (c) topography of annealed sample, and (d) phase of annealed sample.

4. DISCUSSION

4.1. Enhancing Ni-centered clusters by Y substitution in Al-Ni-Gd glasses

As observed in our earlier work [8], with increasing Ni content c_{Ni}, the shoulder peak increases in XRD patterns of as-spun samples, which is ascribed to the enhancement of Al-Ni bonds. In present work, the Ni-Ni bond in the glasses and melts has a similar first neighboring distance r_{max} to the Al-Ni bond and the $g_{Ni\text{-}Ni}(r_{max})$ of the glass with yttrium content c_Y = 6 at.% is much higher than that with c_Y = 0; while both glasses have a similar $g_{Al\text{-}Ni}(r_{max})$ because they have the same c_{Ni} (Fig. 2 and Table 2). Hence, it is inferred that the increment of shoulder peak in the XRD patterns of present glasses with increasing c_Y is mainly associated with the Ni-Ni bonds. Here, the higher first peak in the $g_{Ni-Ni}(r)$ of the glass with c_Y = 6 at.% indicates a stronger linking of Ni-centered clusters. In a glass or melt, the longer the nearest neighboring distance it has, the larger coordinate number it possesses [23]. The change of the bond length of Ni-Ni (Δr = -0.13 Å) in the glass with c_Y = 6 at.% when cooling from the melt is more negative than that with c_Y = 0 (Δr = -0.07 Å) and Al-Ni bonds have the same changing tendency (Δr = -0.04 Å with c_Y = 6 at.% → Δr = -0.03 Å with c_Y = 0), which implies that the coordinate number Z of Ni-centered clusters is increased with Y substitution.

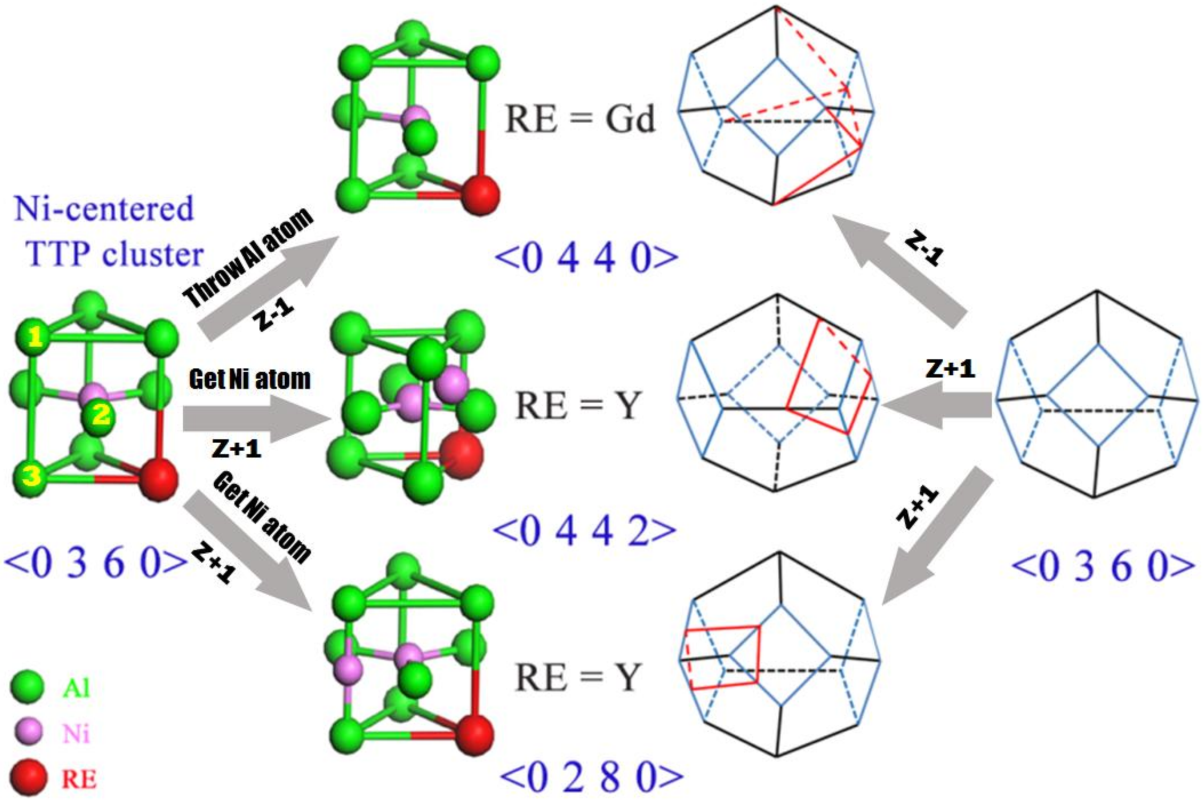

Figure 9. Schematic presentation of the evolution of Ni-centered tri-capped trigonal prism (TTP) clusters to the distorted TTPs. Sites 1 and 3 denote the vertices of the trigonal prism, and site 2 denotes the side atoms of the trigonal prism. When the RE atom is Gd, the TTP tends to throw an Al atom away at site 2 (Z = Z-1) and the corresponding Voronoi polyhedron will add a quadrangle and lose two pentagons to become the index of <0 4 4 0>; when the RE atom is Y, the TTP will capture a Ni atom (Z = Z-1) and if the Ni atom is between the sites 1 and 2, the corresponding Voronoi polyhedron will add a quadrangle and two hexagons and lose two pentagons to become the index of <0 4 4 2> polyhedron, or the Ni atom is between the sites 1 and 3, the corresponding Voronoi polyhedron will lose a quadrangle and add two pentagons to become the index of <0 2 8 0> polyhedron.

Moreover, the Ni-centered tri-capped trigonal prism (TTP) clusters are dominated in the present melts or glasses (Fig. 3a). TTP clusters with Voronoi indices of <0 3 6 0> can link into a network/backbone structure to stabilize the glasses [18, 24]. Here, the population of <0 3 6 0> in glass with c_Y = 6 at.% is much higher than that with c_Y = 0. Furthermore, the glass or melt with c_Y = 6 at.% has more <0 2 8 0> and <0 4 4 2> clusters, which are considered as distorted TTP clusters by capturing one atom and increasing coordinate number (Z = Z+1), and less <0 4 4 0> clusters which can be regarded as the distorted TTP clusters by throwing one atom and decreasing coordinate number (Z = Z-1) [18]. Meanwhile, <0 4 4 0> clusters with c_Y = 6 at.% has a low population of clusters with composition of (7, 0, 1), but a higher population of (8, 0, 0) (Fig. 3c), indicating that Y disfavors joining <0 4 4 0> clusters compared with Gd atom; the situation of <0 3 6 0> and <0 4 4 2> clusters is opposite (Fig. 3b and d). It is explained that the glass with c_Y = 6 at.% has a higher population of <0 3 6 0> clusters but a lower population of <0 4 4 0> clusters than that with c_Y = 0 (Fig. 3a).

If we choose the regular Ni-centered <0 3 6 0> TTP cluster with the most popular composition of (8, 0, 1) as a starting cluster, the distortation of <0 3 6 0> TTP can be schematically shown in Fig. 9. The left half gives the real atomic distribution in the TTP clusters and the right half gives the equivalent clusters using the Voronoi polyhedra. The latter can reflect the change of the Voronoi indexes clearly.

When the RE atom is Gd, <0 3 6 0> cluster tends to lose one Al atom at site 2 and form the <0 4 4 0> polyhedron with a new composition of (7, 0, 1); when RE comes to Y, it will capture a Ni atom between sites 1 and 2 and form <0 4 4 2> polyhedron with a new composition of (8, 1, 1) or add a Ni atom between sites 1 and 3 and form <0 2 8 0> polyhedron. The icosahedronlike polyhedron <0 4 4 2> usually has dense atomic packing with the maximal overlapping of valence electron density and prefers to connect with other clusters and form backbone clusters [18, 24]. Such evolution of TTPs can explain the segregation of Ni atoms and the change of $g_{\text{Ni-Ni}}(r)$ in Fig. 2. Combining XRD patterns and MD simulation as well as the fact that c_{Ni} is constant in present alloys, we may conclude that Y substitution can enhance the segregation tendency of the Ni-centered backbone clusters. The stabilization of Ni atoms by Y addition was also found in Zr-based glasses [25].

In contrast to the strong, disordered and stable Ni-centered clusters, the Al inclusion clusters are considered as crystal-like and active clusters in the Al-based glasses [6, 15, 24]. They are crystallized at a lower temperature during annealing, i.e. the first peak in DSC curves corresponds to the formation of fcc-Al and the second and third peaks are often related to the Ni-rich phases [16, 17]. Since Y substitution can enhance the segregation of Ni-centered clusters, it is understood that $\Delta H_2 + \Delta H_3$ with c_Y = 6 at.% is higher (Table 1). The stronger Ni-centered clusters in the melt with c_Y = 6 at.% should lead to a higher viscosity, and it is expected that the ribbon with c_Y = 6 at.% is thicker than that with c_Y = 0 (Table 1 and Fig. 5).

4.2. Ordering Al-rich clusters by Y substitution in Al-Ni-Gd glasses

In the simulated $g_{\text{Al-Al}}(r)$, Al-Al bonds of the glass with c_Y = 6 at.% shows an expansion after solidifying from the melt (bond length difference Δr = -0.06 Å), but Al-Al bonds with c_Y = 0 remain unchanged (Δr = 0.00 Å). This difference is similar to that of Al-Ni and Ni-Ni bonds after solidification (Table 2). According to Gaskell’s argument [6], the expansion of Al-Al bonds in the glass with c_Y = 6 at.% can increase the coordinate number of Al-rich inclusion clusters; meantime, the $r_{\max}$ of Al-Al bond is closer to that of fcc-Al crystal ($r_{\max}$ = 2.86 Å [26]) compared with c_Y = 0. Combining the crystal-like character of Al-rich clusters [6] and the existence of quench-in fcc-Al nuclei in Al-based glasses [27], it is understood that the Al phase can crystallize easier in the yttrium substituted samples and the first crystallization enthalpy (ΔH_1) decreases with increasing c_Y (Fig. 1b and Table 1). It is also explained that fcc-Al peak in the XRD patterns after annealing treatment tends to increase with increasing c_Y (Fig. 7).

In Al-based metallic glasses, the precipitated crystalline phases even the medium range orders have great influence on the corrosion resistance [2, 28]. It is proposed that nanoscale crystals would have effect on the pit initiation and metastable propagation [2]. During the electrochemical polarization, the ordered Al clusters in sample with c_Y = 6 at.% can supply more active sites to form a thicker Al_2O_3 passive film, leading to a lower passive density (i_{pass}) (Fig. 4a and 7b), a higher intensity of Al 2p XPS spectrum and higher c_{Al} and c_O in their matrix EDS results (Figs. 5 and 6). Hence, the thicker Al_2O_3 film in the sample with c_Y = 6 at.% is possibly the main factor to hide Ni 2p peak in the XPS spectrum (in considering of the limitation of test depth of the XPS equipment), and such absence of Ni 2p peak in XPS test has been reported earlier [25, 29].

4.3. Aggravating the metastable pitting in Al-Ni-Gd glasses

As indicated in Ref.[20, 30], metastable pitting represents the formation of metastable pits which initiate and grow or propagate briefly at the potential below the pitting potential and show a repassivation behaviour; in the potentiostatic current-time (*i-t*) curves of the stainless steel, the metastable pit transients rise slowly, decay quickly, and appear as asymmetrical current “spikes”, indicating that the metastable pits are hard to nucleate but easy to passivate. The review article of Szklarska-Smialowska [19] denotes that the metastable pitting events occur more frequently at potentials closer to the pitting potential and the number of metastable pits on pure Al increases with increasing Cl^- concentration. In article of Burnstein et al. [30], the metastable pitting current transients can be detected with microelectrode. In the work of Böhni et al. [31], there exist many sharp current transients in potentiodynamic curve of stainless steel from microelectrode measurements (d_{cell} = 150 μm), while only a current peak below pitting potential in case of normal electrode (d_{cell} = 10000 μm), indicating the overlap of the current transients. Beside the microelectrode technique, lowering the potentiodynamic scanning rate is other method to reveal the metastable pitting current transients [12, 32]. The potentiadynamic curves of pure iron and mild steel with scanning rate of 0.1 mV/s exhibits typical current transients, the number of which tends to rise with increasing the potential. The polarization curves of the alloy with c_Y = 6 at.% at a scanning rate of 0.1 mV/s shows the metastable pitting current transients (inset in Fig. 4a), which is consistent with the above mentioned literature. Hence, the current peak just below the pitting potential is related to the metastable pitting.

The fcc-Al can act as the initiation point of the local corrosion due to its low stability [2, 33, 34]. The Y substitution can induce more ordered Al-rich clusters and fcc-Al quench-in nuclei. Consequently, it is expected that the metastable pitting peak of the sample with Y substitution initiates earlier and rises higher (Fig. 4a and Table 4) and that the sample with c_Y = 6 at.% has a higher oxygen content after polarization stopped at point β (inset in Fig. 5). During the polarization, the higher standard equilibrium electrode potentials (SEEP) of Ni/Ni^{2+} (-0.25 V_{SHE}) than Al/Al^{3+} (-1.66 V_{SHE}),

Gd/Gd^{3+} (-2.88 V_{SHE}) and Y/Y^{3+}(-2.10 V_{SHE}) [35, 36] cause nickel to resist the electrochemical polarization in a local area. When dealloying Cu-rich and Au-rich metallic glasses, the selective dissolution of elements can introduce stress and lead to cracks [37, 38]. Our earlier work shows that Ni acts as a dissolution moderator to block the further corrosion of the pitting hole and the stronger Ni-centered clusters exist, the larger stress are induced and the more developed cracks and higher P_{mp} are formed [8]. Hence, the sample with c_Y = 6 at.% after full polarization and polarization till β point has more flower-like cracks than the sample with c_Y = 0 (Fig. 5). Obviously, the spalling of the fragments induced by stress will further increase the pit current. Consequently, enhancing Ni-centered clusters by Y substitution is another reason for a more negative onset potential E_x of P_{mp} and a higher $\bar{i}_{mp}$ with a higher c_Y (Fig. 4 and Table 4). Since the Ni-centered clusters in the glass with c_Y = 6 at.% have a larger segregation degree, it is expected that the fork-like crack appears and the size of each single flower-like crack zone is larger compared with the glass with c_Y = 0 (Fig. 5).

As shown in XRD and AFM investigations (Figs. 7a and 8), the Al-rich clusters are ordered and fcc-Al are devitrified after annealing treatment. According to the low stability of fcc-Al in local corrosion [33, 34], it is expected the P_{mp} of annealed samples occurs earlier and grows higher compared with the as-spun samples (Table 4). It is also understood that the Al and O contents deduced from the XPS spectrums of the annealed sample with c_Y = 0 after polarization are higher compared with the as-spun sample (Table 3). Meanwhile, the bright zones (Ni-rich phase) in AFM phase image grow after the annealing treatment (Fig. 8). Considering the effect of yttrium on P_{mp} and sample surface composition, the annealing treatment has a similar effect on the clusters to the Y substitution, i.e. the Ni-centered cluster as well as the induced corrosion stress can be strengthened by not only Y substitution but also annealing treatment. Moreover, the devitrification shrink of a glass can induce stress in the glass matrix [39]. Hence, the inner stress due to the volume shrink and Ni-centered cluster strengthening in the annealed sample can also lead to an earlier and higher P_{mp} peak (Fig. 7b and Table 4). Indeed, annealing treatment on the Al-Ni-Y and Al-Co-Ce glasses can make the initiation of their metastable pitting easier [29, 33]. In other words, the annealing treatment, similar to Y substitution, can aggravate the metastable pitting due to the ordering of Al clusters and the segregation of Ni-centered clusters.

5. CONCLUSIONS

The corrosion behaviour of $Al_{84}Ni_{10}Gd_{6-x}Y_x$ (x = 0, 2, 4 and 6) metallic glasses has been studied in the amorphous and partially devitrified states in 3.5 wt.% NaCl solution by the polarization test. Meantime, the thermodynamic parameters, atomic cluster evolution, surface information of samples have been investigated. The relationship between the evolution mechanism of the TTP clusters and Y substitution are discussed. We find:

1) With substituting Gd by Y, the shoulder peak in XRD patterns of Al-based glasses, the enthalpy of second and third crystallization (ΔH_2+ΔH_3) and the thickness of as-spun samples increase. Meantime, the $g_{Ni\text{-}Ni}(r_{max})$ of Ni-Ni bonds and population of <0 3 6 0> and <0 4 4 2> Ni-centered clusters in the glass with c_Y = 6 at.% are higher compared with the glass with c_Y = 0. These results

indicate that Y substitution can enhance the segregation of Ni-centered clusters in present Al-based glasses.

2) With Y substitution, the onset temperature and the first crystallization enthalpy (ΔH_1) decrease gradually. Besides, the Al 2p XPS peak and the matrix O content of the corroded sample with c_Y = 6 at.% are higher compared with c_Y = 0, indicating that Y substitution can enhance the order of Al-rich inclusion clusters in present glasses. And the AFM images indicate that annealing treatment can increase the size of the Al-rich region or cluster.

3) With gradual Y substitution, the onset potential E_x of the metastable pitting peak P_{mp} becomes more negative, and the height $\bar{i}_{mp}$ of P_{mp} increases. The cracks of the corroded sample with c_Y = 6 at.% is more developed than that with c_Y = 0. These results suggest that Y substitution can enhance the corrosion stress due to the ordering of Al-rich clusters and the segregation of Ni-centered clusters. Meanwhile, annealing treatment has a similar effect to Y substitution.

4) The role of Y substitution on the segregation of Ni-centered clusters can be explained by a new proposed mechanism: when containing one Y atom, the <0 3 6 0> Ni-centered cluster prefers to capture one Ni atom, inducing the segregation of Ni-centered clusters and formation of the backbone clusters; when containing one Gd atom, it prefers to throw one Al atom and weaken the backbone clusters in the Al-based glasses. This mechanism is helpful to understand the metastable pitting behaviour and to design new corrosion resistant Al-based glasses.

ACKNOWLEDGEMENTS

The authors thank Mr. W.J. Zhang in Wuhan Corrtest Instruments Company for conducting the potentiodynamic scanning test on the sample with 0.1 mV/s. We acknowledge the National Natural Science Foundation of China (Nos.51171091, 51471099, 51571132) and National Basic Research Program of China (973 Program) (No.2012CB825702) for financial supports.

References

1. F. Presuel Moreno, M.A. Jakab, N. Tailleart, M. Goldman, J.R. Scully, *Materials Today*, 11 (2008) 14-23.
2. S.D. Zhang, Z.M. Wang, X.C. Chang, W.L. Hou, J.Q. Wang, *Corros. Sci.*, 53 (2011) 3007-3015.
3. A. Mansour, C.-P. Wong, R. Brizzolara, *Phys. Rev.* B, 50 (1994) 12401.
4. Y.G. Wang, Y. Liu, Y.J. Li, B. An, G.H. Cao, S.F. Jin, Y.M. Sun, W.M. Wang, *J. Mater. Sci. Technol.*, 30 (2014) 1262-1270.
5. H.W. Sheng, Y.Q. Cheng, P.L. Lee, S.D. Shastri, E. Ma, *Acta Mater.*, 56 (2008) 6264-6272.
6. S.J. Poon, G.J. Shiflet, F.Q. Guo, V. Ponnambalam, *J. Non-cryst. Solids*., 317 (2003) 1-9.
7. J.J. Han, W.Y. Wang, C.P. Wang, X.D. Hui, X.J. Liu, Z.K. Liu, *Intermetallics*, 46 (2014) 29-39.
8. G.H. Li, S.P. Pan, J.Y. Qin, Z.H. Zhang, W.M. Wang, *Corros. Sci.*, 66 (2013) 360-368.
9. J.J. Lewandowski, *Mater. Trans*., 42 (2001) 633-637.
10. T. Egami, *Mater. Res. Bull*., 13 (1978) 557-562.
11. S.D. Zhang, Z.W. Liu, Z.M. Wang, J.Q. Wang, *Corros. Sci*., 83 (2014) 111-123.
12. H. Wang, J. Xie, K.P. Yan, M. Duan, Y. Zuo, *Corros. Sci*., 51 (2009) 181-185.
13. G. Kresse, J. Furthmüller, *Comp. Mater. Sci*., 6 (1996) 15-50.
14. J.E. Sweitzer, G.J. Shiflet, J.R. Scully, *Electrochim. Acta*, 48 (2003) 1223-1234.
15. L. Wang, H.R. Cong, J.X. Zhang, X.F. Bian, H. Li, J.Y. Qin, *Phys. Lett*. A, 301 (2002) 477-483.

16. M.C. Gao, G. Shiflet, *Scripta Mater.*, 53 (2005) 1129-1134.
17. A. Tsai, T. Kamiyama, Y. Kawamura, A. Inoue, T. Masumoto, *Acta Mater*., 45 (1997) 1477-1487.
18. P.F. Guan, T. Fujita, A. Hirata, Y.H. Liu, M.W. Chen, *Phys. Rev. Lett*., 108 (2012) 175501.
19. Z. Szklarska Smialowska, *Corros. Sci*., 41 (1999) 1743-1767.
20. G. Frankel, *J. Electrochem. Soc*., 145 (1998) 2186-2198.
21. S.F. Y. Zuo, *Corros. Sci.*, 39 (1997) 465-471.
22. S. Magonov, V. Elings, M.-H. Whangbo, *Surf. Sci*., 375 (1997) L385-L391.
23. P.H. Gaskell, *J. Non-cryst. Solids*., 192–193 (1995) 9-22.
24. P. Gaskell, *J. Non-cryst. Solids*., 32 (1979) 207-224.
25. A. Kawashima, K. Ohmura, Y. Yokoyama, A. Inoue, *Corros. Sci*., 53 (2011) 2778-2784.
26. D. Feng, Metal Physics (first volume : structure and defect), in, Science Press, Beijing, 2000.
27. Y. Liu, S.L. Ye, B. An, Y.G. Wang, Y.J. Li, L.C. Zhang, W.M. Wang, *J. Alloy. Compd.*, 587 (2014) 59-65.
28. J. Sweitzer, J. Scully, R. Bley, J. Hsu, *Electrochemical and solid-state letters*, 2 (1999) 267-270.
29. R. Jindal, V. Raja, M. Gibson, M. Styles, T. Bastow, C. Hutchinson, *Corros. Sci*., 84 (2014) 54-65.
30. G. Burstein, C. Liu, R. Souto, S. Vines, *Corrosion Engineering, Science and Technology,* 39 (2004) 25-30.
31. H. Böhni, T. Suter, A. Schreyer, *Electrochim. Acta,* 40 (1995) 1361-1368.
32. Y. Tang, Y. Zuo, J. Wang, X. Zhao, B. Niu, B. Lin, *Corros. Sci.*, 80 (2014) 111-119.
33. N. Tailleart, R. Huang, T. Aburada, D. Horton, J. Scully, *Corros. Sc*i., 59 (2012) 238-248.
34. A.M. Lucente, J.R. Scully, *J. Electrochem. Soc*., 155 (2008) C234-C243.
35. T. Moeller, H.E. Kremers, *Chem. Rev*., 37 (1945) 97-159.
36. X.D. Bai, Corrosion and Control of Materials, in, Beijing: Tsinghua University Press, 2005.
37. Z.F. Zhao, J. Xu, P.K. Liaw, B. Wu, Y. Wang, *Corros. Sci*., 84 (2014) 66-73.
38. F. Scaglione, A. Gebert, L. Battezzati, *Intermetallics*, 18 (2010) 2338-2342.
39. L. Li, B. Kharas, H. Zhang, S. Sampath, *Materials Science and Engineering*: A, 456 (2007) 35-42.